Applied Physics A (2022) 128:439
https://doi.org/10.1007/s00339-022-05580-3

Applied Physics A
Materials Science & Processing

Effect of Bi_2O_3–B_2O_3 as a sintering aid in microstructure and dielectric properties of $Fe_2Mo_3O_{12}$ electroceramic

Eduardo Viana de Araújo[1] · Marcelo Antonio Santos da Silva[2] · Mauricio Sousa de Pereira[3] · Antonio Sérgio Bezerra Sombra[2] · Igor Frota de Vasconcelos[3] · Pierre Basílio Almeida Fechine[1]

Received: 16 March 2022 / Accepted: 6 April 2022 / Published online: 26 April 2022

Abstract
Molybdates from $A_2Mo_3O_{12}$ family have been widely investigated due to its low sintering temperature, low thermal expansion coefficient, and low dielectric loss. $Fe_2Mo_3O_{12}$ (FMO) is an oxide from this family and widely used in the catalytic field. The aim of this work is to evaluate the influence of the Bi_2O_3–B_2O_3 as a sintering aid in the microstructure and dielectric properties of FMO. The diffraction results showed that the FMO with the monoclinic structure phase was obtained after the calcination process (650 °C). Mössbauer spectroscopy showed the formation of Fe_2O_3 after the sintering process at 800 °C. The scanning electron-microscopic image demonstrates an increase of the grain as a function of sintering aid concentration. The samples were analyzed using the impedance spectroscopy at radiofrequency with temperature variation. The Nyquist diagram obtained in this temperature range was fitted from an equivalent circuit with three R-CPE associations, corresponding to the morphology of the electroceramics. For dielectric properties in the microwave, all the samples showed values of ε_r lower than 10. Values of $Q\,x\,f$ above 14,132.35 GHz were achieved. The thermal stability was evaluated by the temperature coefficient of resonant frequency (τ_f). The lowest τ_f values of − 6.55 ppm/°C and − 4.35 ppm/°C (near-zero) were measured to FMO and FMO mixed with 7.5 wt % Bi_2O_3–B_2O_3, respectively. Based on these results, FMO can be used to low-permittivity ceramic for low-temperature co-fired ceramics (*LTCC)* applications, antenna substrate, and millimeter-wave range.

Keywords LTCC · $Fe_2Mo_3O_{12}$ · Microwave · Impedance spectroscopy

1 Introduction

The electroceramics emerged as an excellent option for integration and miniaturization of electronic circuits, making smaller and more efficient systems [1]. Due to the advances in telecommunications, it is required that the materials have appropriated dielectric constant (ε_r), low dielectric loss (*tan* δ), near-zero temperature coefficient of resonant frequency (τ_f), high-quality factor ($Q\,x\,f$), temperature stable and versatile [2, 3]. Electroceramics are widely used in the manufacturing of microwave electronic devices, dielectric substrates, resonators owing to their easy integration in chips [4]. Most of these ceramics require high sintering temperature, which can be a factor that hinders the integration of them into an

✉ Pierre Basílio Almeida Fechine
fechine@ufc.br

Eduardo Viana de Araújo
eduardo.qufc@gmail.com

Marcelo Antonio Santos da Silva
marceloassilva@yahoo.com.br

Mauricio Sousa de Pereira
mauriciosousa@alu.ufc.br

Antonio Sérgio Bezerra Sombra
asbsombra@gmail.com

Igor Frota de Vasconcelos
ifvasco@ufc.br

[1] Grupo de Química de Materiais Avançados (GQMat), Departamento de Química Analítica e Físico-Química, Universidade Federal do Ceará–UFC, Campus do Pici, CP 12100, Fortaleza, CE CEP 60451-970, Brazil

[2] Laboratório de Telecomunicações e Ciência e Engenharia de Materiais (LOCEM), Departamento de Física, Universidade Federal Do Ceará, Fortaleza, Brazil

[3] Laboratório de Materiais Avançados, Departamento de Engenharia Metalúrgica e de Materiais, Universidade Federal Do Ceará, Fortaleza, Brazil

electronic circuit [5]. Therefore, low-temperature co-fired ceramics (LTCC) were developed by adding low quantities of melting temperature oxides, such as Bi_2O_3 [2, 6], B_2O_3 [7], V_2O_5 [8], among others [9, 10], which allows the sintering process below 950 °C.

Recent studies point MoO_3 based electroceramic as an excellent option for *LTCC* application [11–15], with high $Q\ x\ f$ and low $tan\ \delta$. Nina Joseph and coworkers obtained $CuMoO_4$ sintered at low temperature and completely compatible with the Al electrode and with $Q\ x\ f$ of 53,000 GHz and ε_r of 7.9 [16]. Li-xia Pang et al.obtained $(K_{0.5}La_{0.5})MoO_4$ with middle ε_r, $Q\ x\ f$ of 59,000 GHz, and 0.0002 of $tan\ \delta$ [17]. However, *LTCC* molybdate based materials have high τ_f values [2, 5, 18, 21, 23] and the addition of other compounds are necessary to shift the τ_f to near-zero values. Nina Joseph and coworkers added Ag_2O in $CuMoO_4$ ($\tau_f = -36$ ppm.°C^{-1}) to achieve composite with near-zero τ_f [19].

Molybdates belonging to $A_2M_3O_{12}$ family, where A is a trivalent cation (Fe^{3+}, Al^{3+}, Y^{3+}, and other rare earths) and M is a hexavalent cation (Mo^{6+} or W^{6+}). They have been widely investigated due to their negative or near-zero thermal expansion coefficient (α): $Y_2Mo_3O_{12}$ [20], $Al_2Mo_3O_{12}$ [2], $Sc_2Mo_3O_{12}$ [21], $Fe_2Mo_3O_{12}$ [22], $HfMgW_3O_{12}$ [23], $In_2W_3O_{12}$ [24], $Al_2W_3O_{12}$, $Sc_2W_3O_{12}$ [25], among others. The iron (III) molybdate ($Fe_2Mo_3O_{12}$) has a monoclinic structure at room temperature and shows a monoclinic-to-orthorhombic transition between 510 and 520 °C [26, 27]. Li, Z.W, and coworkers [28] had investigated the $Fe_2Mo_3O_{12}$ (FMO) and they observed the low α of this phase. This property is desirable in the development of electronic devices, where it is needed a material which its dimensions do not change with the temperature changing [29].

FMO has been using to degradation reactions, for rhodamine-B using photocatalyst process, for example [30]. However, the application of FMO, as a potential *LTCC*, has never been made so far to our knowledge. In this sense, a Bi_2O_3–B_2O_3 mix is used as a sintering aid, the liquid phase of Bi_2O_3 allows the grain growth during the sintering process [32, 33], while B_2O_3 is usually employed as flux former [33]. Therefore, the purpose of this study was to evaluate the effect of Bi_2O_3–B_2O_3 mix in the microstructure, structure phase, and dielectric properties at radiofrequency and microwave range of FMO electroceramics.

2 Methodology

FMO electroceramic was synthesized by solid-sate route using Fe_2O_3 (99%, Sigma Aldrich) and MoO_3 (99.5%, Sigma Aldrich). These starting materials were ground and mixed in agate mortar following the stoichiometry, as described in Eq. 1.

$$Fe_2O_{3(s)} + 3\,MoO_{3(s)} \rightarrow Fe_2Mo_3O_{12(s)} \quad (1)$$

The mixture was pressed into pellets and calcinated at 650 °C for 16 h. The Bi_2O_3–B_2O_3 sintering aid was prepared using Bi_2O_3 (99.9%, Sigma Aldrich) and B_2O_3 (98%, Sigma Aldrich) and was added in molar ratio 1:1 and mixed in Fritsch Pulverisette 6 planetary mill for 10 h with 370 rpm as rotation speed. Milling was performed in sealed stainless-steel vials under air with stainless-steel balls. A ball mass ratio of 1:9 (Bi_2O_3–B_2O_3 powder mass: ball mass) was used.

For dielectric characterization, the samples were ground and mixed with a binder: polyvinyl alcohol (PVA) 10% v/v solution. Bi_2O_3–B_2O_3 was added as sintering aid and the samples were labeled as FMO-X (X = 2.5, 5.0 and 7.5 wt% Bi_2O_3–B_2O_3). Then, each composition was pressed into cylindrical pellets and sintered at 800 °C for 6 h. The volume of these pellets was determined by Archimedes' method to calculate their density. These pellets were polished on both faces and a silver paste (Joint Metal-PC200) was applied on them to ensure the electrical contact.

Powder X-ray diffraction (PXRD) patterns were obtained using a PANalytical diffractometer (Xpert Pro MPD) operating at 40 kV and 40 mA in the Bragg–Brentano geometry, with a Co tube (Ka_1: 1.7889 Å). The diffraction patterns were collected at room temperature from pulverized FMO calcinated and sintered samples. The diffractograms were obtained from 10° to 60° at a step size of 0.013°, with an analysis time of 70 s at each step, in a graphite monochromator in the plane geometry for diffracted beam.

Mössbauer spectra were obtained using transmission mode at room temperature. The ^{57}Co radioactive source in Rh matrix was used mounted in speed controller scanning from -10 mm.s^{-1} to $+10$ mm.s^{-1} [34]. Spectra were also obtained for FMO calcinated and sintered samples.

Raman spectra were obtained using LabRAM Jobin–Yvon HORIBA spectometer, equipped with liquid nitrogen cooled CCD. A Laser beam was focused in the sample surface using OLYMPUS microscope lens and numeric opening of 0.75, forming a spot of 4 μm^2 under the sample surface. The slits were adjusted to obtain a resolution of 2 cm^{-1}.

The surface's microstructure of the FMO based electroceramics was studied by scanning electron microscopy (SEM). Micrograph images were collected at room temperature using a FEG Quanta 450 with Energy-dispersive X-ray spectroscopy (EDS) in the SEM chamber, with an incident electron beam of 20 kV. The average grain size was determined using ImageJ software [35], from at least 50 particles measurements.

For dielectric measurements at the RF range, the samples were evaluated using a Solartron 1260 computer-controlled impedance analyzer as a function of frequency (1 Hz–10 MHz) at different temperatures (220–260 °C). On the other hand, the dielectric measurements for the

microwave range were evaluated with an Agilent Model PNA N5230A using the Hakki-Coleman method [36]. The Agilent PNA N5230A was also used to measure the τ_f of the FMO as described by Silva and his coworkers [37].

3 Results and discussion

To confirm the complete calcination of FMO and achieve the crystalline phase, all the samples were analyzed by PXRD technique and compared to $Fe_2Mo_3O_{12}$ (ICSD: 100,606, monoclinic, $P2_1/a_1$) crystalline phase. Figure 1a shows the diffraction pattern of the $Fe_2Mo_3O_{12}$ based ceramics. The

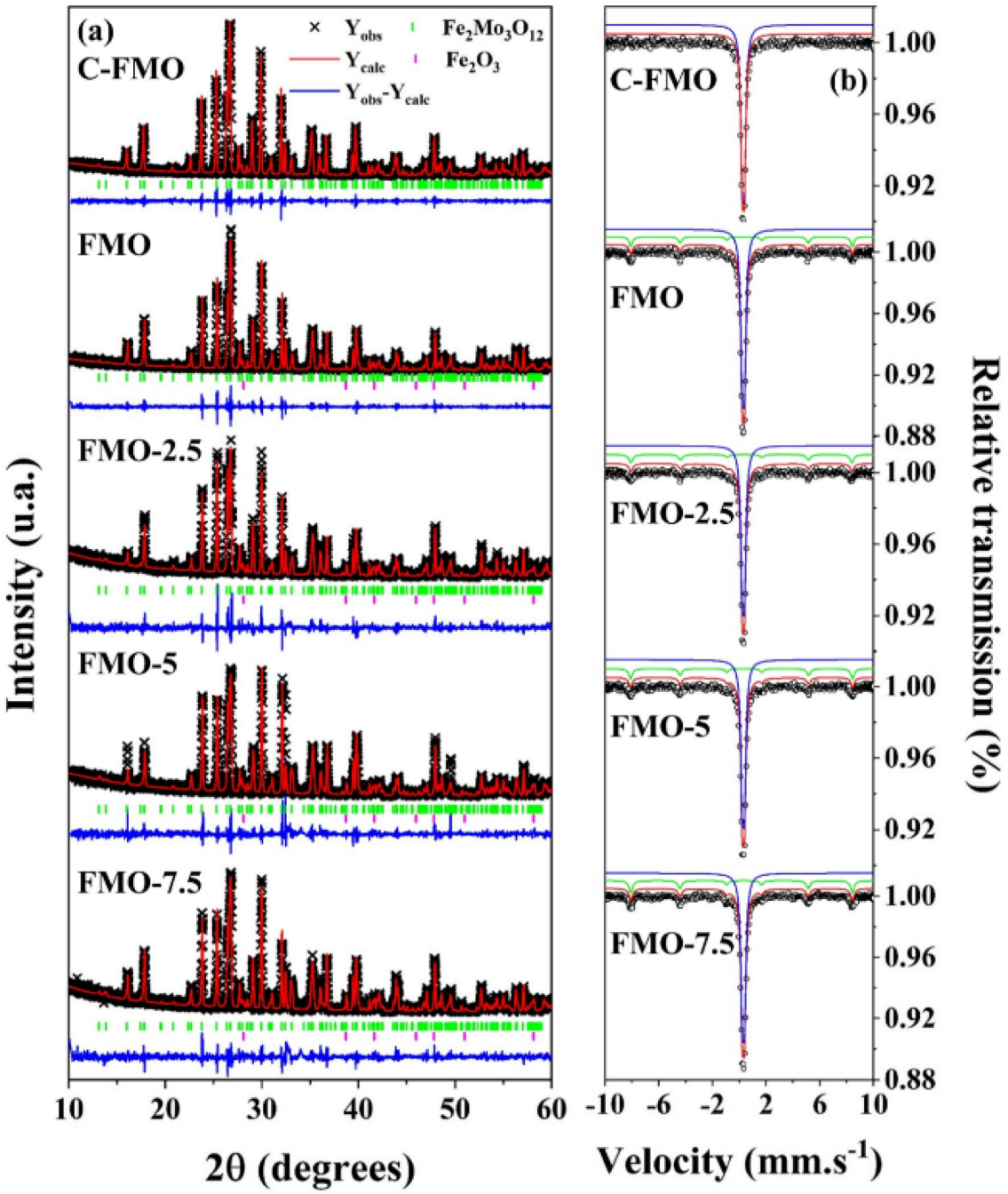

Fig. 1 Rietveld refinement of the PXRD **a** with observed (Y_{Obs}) and calculated (Y_{Calc}) intensities and Mössbauer spectra **b** of C-FMO, FMO, FMO-2.5, FMO-5.0 and FMO-7.5

first diffractogram is relative to $Fe_2Mo_3O_{12}$ after calcination process and before sintering process (C-FMO). For this sample, only monoclinic $Fe_2Mo_3O_{12}$ was achieved. For FMO sintered and sintering aid added samples, the results demonstrated that a fraction (from 2.2 at 20 wt %) of Fe_2O_3 (ICSD: 154,190) spurious phase is formed. This behavior was observed for all sintered samples, being also observed a mass loss in all pellets. Prisco et al. related that $A_2Mo_3O_{12}$ molybdates has a thermic decomposition in temperatures higher than 700 °C, forming initial oxides used in the reaction [38]. Therefore, all sintered samples were also analyzed by PXRD to examine the crystalline structure after the sintering process. Diffractograms of FMO, FMO-2.5, FMO-5.0 and FMO-7.5 presented the formation of Fe_2O_3 (ICSD: 154,190, Rhombohedral, R-3c) phase, confirming the thermal decomposition of $Fe_2Mo_3O_{12}$ after the sintering process as described in Eq. 2.

$$Fe_2Mo_3O_{12(s)} \rightarrow Fe_2O_{3(s)} + 3\,MoO_{3(s)}. \quad (2)$$

In the literature, Bi_2O_3–B_2O_3 mixture acts as a sintering aid formed an amorphous compound after thermal process [31, 39]. In this work, no peaks relative to these phases (Bi_2O_3 or B_2O_3) were found in diffractograms.

Rietveld refinement parameters are presented in Table 1. Low values of agreement indices for all samples shows that the Rietveld refinements were satisfactory, with weighted profile R-factor (R_{WP}) below 20% or between 20 and 30% for samples with two or more phases and χ^2 near to unity [40]. Another factor is the similarity between lattice parameters of samples and the pattern of database, which indicates that structure did not change with addition of Bi_2O_3 and B_2O_3, since Bi^{3+} can substitute Fe^{3+} in octahedral site [41].

The Mössbauer spectra of the samples are shown in Fig. 1b. All samples showed a doublet with isomer shift (δ) near to 0.41 mm/s, related to paramagnetic Fe^{3+} ion in high spin state and quadrupole splitting (Δ) at 0.18 mm/s, which is assigned to [FeO_6] sites in $Fe_2Mo_3O_{12}$ monoclinic phase [42]. Spectra of sintered samples showed a low intensity simple sextet, indicating a magnetically ordered state. The high value of hyperfine field (B_{HF}) (above 51 T), and the values of δ near 0.37 mm/s indicates the presence of α-Fe_2O_3 phase [43–45], which were also found in PXRD analysis. The experimental data of hyperfine parameters are presented in Table 2.

As discussed in PXRD, Fe_2O_3 content rise as sintering aid content rise according to area (%) values presented in Table 1. No Fe_2O_3 was observed in C-FMO spectrum, since it was not sintered, while FMO-7.5 presented 18.4% of Fe_2O_3. However, in the 7.5 wt % of Bi_2O_3–B_2O_3 a drop in iron oxide concentration is observed in PXRD when compared to Mössbauer spectra. This phenomenon can

Table 1 Agreement indices and lattice parameter for $Fe_2Mo_3O_{12}$ based ceramics

Sample	Phase	Composition (%)	Lattice parameters							R_{WP} (%)	χ^2
			a (Å)	b (Å)	c (Å)	V (Å^3)	α (°)	β (°)	γ (°)		
C-FMO	$Fe_2Mo_3O_{12}$	100	15.6949 (3)	9.2357 (1)	18.2226 (4)	2157.68 (7)	90.0	125.228 (1)	90.0	14.68	1.003
FMO	$Fe_2Mo_3O_{12}$	97.8	15.6974 (2)	9.2367 (1)	18.2230 (3)	2158.48 (5)	90.0	125.222 (1)	90.0	15.08	0.973
	Fe_2O_3	2.2	5.4308 (7)	5.4308 (7)	5.4308 (7)	100.73 (2)	55.241 (6)	55.241 (6)	55.241 (6)		
FMO-2.5	$Fe_2Mo_3O_{12}$	88.9	15.6987 (4)	9.2376 (1)	18.2228 (5)	2158.67 (9)	90.0	125.229 (1)	90.0	20.67	1.366
	Fe_2O_3	11.1	5.4268 (1)	5.4268 (1)	5.4268 (1)	100.70 (3)	55.313 (9)	55.313 (9)	55.313 (9)		
FMO-5.0	$Fe_2Mo_3O_{12}$	79.64	15.6992 (4)	9.2374 (1)	18.2226 (5)	2158.96 (9)	90.0	125.218 (1)	90.0	20.13	1.447
	Fe_2O_3	20.36	5.4292 (1)	5.4292 (1)	5.4292 (1)	100.71 (3)	55.266 (9)	55.266 (9)	55.266 (9)		
FMO-7.5	$Fe_2Mo_3O_{12}$	92.9	15.6984 (4)	9.2386 (1)	18.2272 (5)	2159.36 (9)	90.0	125.230 (2)	90.0	18.89	1.242
	Fe_2O_3	7.1	5.4293 (6)	5.4293 (6)	5.4293 (6)	100.74 (2)	55.276 (5)	55.276 (5)	55.276 (5)		

Table 2 Hyperfine parameters for $Fe_2Mo_3O_{12}$ based ceramics. δ, Δ, Γ, B_{HF} are isomer shift, quadrupole splitting, line width and hyperfine field, respectively

Sample		δ (mm/s)	Δ (mm/s)	Γ (mm/s)	B_{HF} (T)	Area (%)
C-FMO	Dublet	0.407	0.177	0.265	–	100
FMO	Dublet	0.408	0.180	0.274	–	86.5
	Sextet	0.369	– 0.193	0.288	51.19	13.5
FMO-2.5	Dublet	0.406	0.178	0.266	–	86.0
	Sextet	0.375	– 0.240	0.327	51.12	14.0
FMO-5.0	Dublet	0.407	0.180	0.260	–	84.4
	Sextet	0.373	– 0.213	0.290	51.30	15.6
FMO-7.5	Dublet	0.408	0.179	0.269	–	81.6
	Sextet	0.366	– 0.188	0.308	51.22	18.4

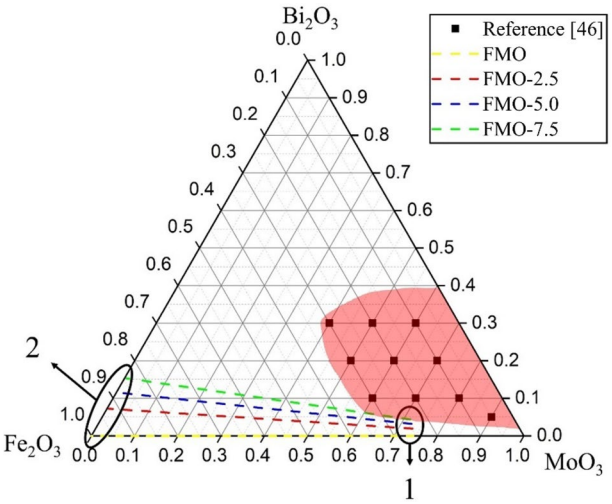

Fig. 2 Ternary diagram for Fe_2O_3-Bi_2O_3-MoO_3 system

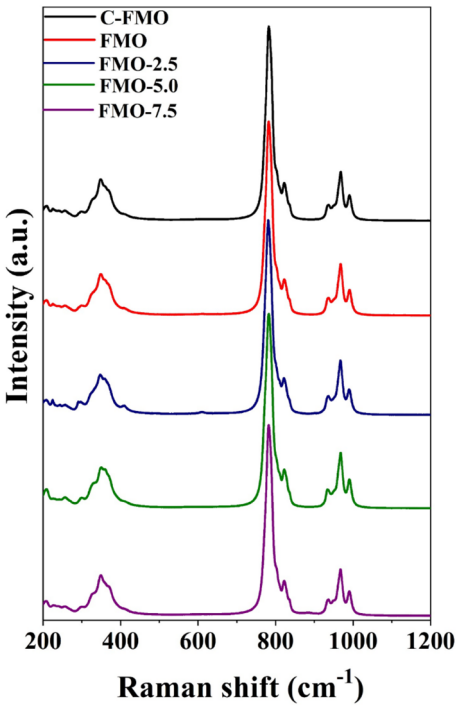

Fig. 3 Raman spectra of C-FMO, FMO, FMO-2.5, FMO-5.0 and FMO-7.5

be explained by a ternary diagram for Fe_2O_3-Bi_2O_3-MoO_3 (Fig. 2). At region 1 of ternary diagram, the samples start to decompose above 700 °C in sintering process and producing this molar ratio for all samples. As temperature increases, MoO_3 volatizes, and the Fe_2O_3 and Bi_2O_3 molar fraction increases for all samples, until reach equilibrium at region 2. When FMO-7.5 decomposes, the molar ratio of Fe_2O_3-Bi_2O_3-MoO_3 system promote the formation of a vitreous phase, as described by Iardanova [46]. PXRD analysis depends on the crystallinity of the sample, but this technique is not able to quantify entire Fe_2O_3, since it is forming an amorphous vitreous phase, but Mössbauer identify the Fe environment. Therefore, Mössbauer spectroscopy is able to quantify the entire Fe quantity.

Figure 3 shows Raman spectra for FMO samples. The $Fe_2Mo_3O_{12}$ monoclinic phase belongs to $P2_1/a_1$ space group with eight molecular formula for unit cell. According to group theory, $Fe_2Mo_3O_{12}$ has 408 modes in Brillouin zone, three of which are acoustic modes and the rest are optical modes which may be described as irreducible representation $\Gamma_{P2_1/a_1} = 102\ A_g + 102\ B_g + 101\ A_u + 100\ B_u$. Only A_g e B_g are Raman active [27]. For FMO sample, main modes of $Fe_2Mo_3O_{12}$ structure are observed, which reinforces the data obtained from PXRD analysis. Raman spectra of sintered sample FMO is similar to C-FMO. Fe_2O_3, Bi_2O_3 and B_2O_3 phases were not assigned due to its bands being overlapped by $Fe_2Mo_3O_{12}$'s spectrum. Regions between 700–900 cm^{-1} and 900–1200 cm^{-1} show that some bands keep their shape, intensity and width as it can be seen in Fig. 3. According to Moura et al. [27] the band within 200–300 cm^{-1} correspond to translational motions of MoO_4 polyhedra, band from 300 to 500 cm^{-1} is related to MoO_4 tetrahedral bendings. Vibrational modes in 783, 803, 822 and 936 cm^{-1} are assigned to asymmetrical stretching of Mo–O bond and modes in 968 e 990 cm^{-1} represents symmetrical stretching of Mo–O bond.

All bands and its correlated vibrational modes are presented in Table S1 in Electronic Supplementary Material (ESM).

After sintering process, the pellets were analyzed by SEM at 1000X magnification. Figure 4a shows the superficial micrograph for FMO. It presents grain size from 2 to 14 µm of diameter and average size of 5 µm, while for FMO-2.5, FMO-5.0 and FMO-7.5 (Fig. 4b–d) are between 6 and 61 µm. The average sizes are 17, 24 and 24 µm for FMO-2.5, FMO-5.0 and FMO-7.5 respectively, as can be seen in the inset of these micrographs. According Tohidifar [31], the sintering aid increases the grain size due the liquid phase flow which promotes the dissolution and diffusion of $Fe_2Mo_3O_{12}$ grains. Although all pellets showed relative density near to 85% ± 2%, which implies that the addition of Bi_2O_3–B_2O_3 as sintering aid does not change the relative density of material in 800 °C sintering process. It was observed in past studies that relative density is dependent of Bi_2O_3 content in sintering aid, as sintering aid content rises in mixture, Bi_2O_3 concentration in sintering aid must decrease to preserve a high relative density [31]. Therefore, a slightly decrease in relative density was expected to be observed since Bi_2O_3 content was kept constant. According to the scanning utilizing EDS technique (Fig. 4e and Fig. S1 in ESM), the surface of all sintered samples are rich in Fe and poor in Mo, which reinforces that thermal decomposition during sintering process volatilizing MoO_3, leaving the Fe_2O_3 on the surface of pellets evidenced by mass loss of 5–10% [38, 47].

The broken pellets were also analyzed to investigate inner composition (inside the pellet) and compare to the surface. Fig. S2 of ESM presents micrograph for all the samples and they showed average grain size near to 20 µm for FMO and 38 µm for the others, higher than those on pellet surface. The scanning using EDS maps are presented in Fig. S3 (ESM) and shows that the concentration of Mo is higher than the ones on surface, which indicates that the pellet's interior does not suffer critical changes in its composition. Table S2 presents the concentration of each element for each sample, for both surface and inside of pellet. Due to the difference on surface and inner composition, EDS analysis of cross section for the FMO sample was made to investigate the inner/surface interface of this material after sintering process and is presented in Fig. 5. Figure 5a shows the EDS spectrum for pellet surface, while Fig. 5b, c presents the EDS spectra for interface and inner, respectively. As can be seen, the amount of Mo is lower on surface than inside the pellet indicating the thermal decomposition of $Fe_2Mo_3O_{12}$ in Fe_2O_3 and MoO_3 and then the MoO_3 volatilization at 700 °C on the surface of the pellet [39, 47–49].

The results of all structural and morphological characterization allow us to affirm that small part of $Fe_2Mo_3O_{12}$ decomposes thermally in MoO_3 and Fe_2O_3. Superficial MoO_3 volatilize and left surface rich in Fe_2O_3 (observed in mass loss after sintering process and EDS analysis), while inner MoO_3 may form an amorphous glass phase with Fe_2O_3 and Bi_2O_3 [46].

Figure 6 shows the imaginary part of impedance (*Z"*) spectra and temperature dependency (220–260 °C) for the samples. For FMO (Fig. 6a), FMO-2.5 (Fig. 6b) and FMO-5.0 (Fig. 6c) there is a peak about 1 MHz, while for FMO-7.5 (Fig. 6d) this peak appears near to 100 kHz. For the maximum of peak observed in *Z*" spectrum is observed a shift for higher values with increasing of the temperature what can be related to the relaxation process thermally activated [50]. As can be seen in insets of Fig. 6, the normalized peaks shift to regions of higher frequency.

The shift is thermally activated and may be described by Arrhenius' equation:

$$\ln f_{Max} = \ln f_0 - \frac{E_a}{k_b T}, \tag{3}$$

where f_{Max} is the frequency when *Z"* has a maximum value, f_o is the pre-exponential term, E_a is the activation energy of the process, K_b is the Boltzmann constant and *T* is temperature [50]. The E_a are determined by the angular coefficient of linear curves in Fig. 7.

The addition of sintering aid has a direct influence on this process. The E_a increases with rising in sintering aid addition, except for FMO-7.5. This increase is probably due to the higher concentration of Bi_2O_3 and Fe_2O_3 spurious phase [51], as seen in PXRD and Mössbauer spectroscopy. FMO presented the lowest E_a value (0.502 eV), since it has the lowest Fe_2O_3 and Bi_2O_3 concentration, while FMO-5.0 has higher quantity of crystalline Fe_2O_3 and Bi_2O_3 and presented the highest value (0.810 eV). However, However, FMO-7.5 has low quantity of crystalline Fe_2O_3 and its E_a is lower than FMO-2.5 and FMO-5.0.

Nyquist's plots (*Z" versus Z'*) were also analyzed. The spectra presented deformed semicircles in relation to *Z"* axis, corresponding to non-Debye model [52]. The behavior of the ceramic material may be described as resistor–capacitor (R–C), equivalent circuit describing the electric response of grain, grain boundary and electrode effect. As the capacitive contribution does not represent an ideal behavior, the capacitor is substituted by a constant phase element (CPE). The CPE impedance (Z_{CPE}) is described as the following equation [50]:

$$Z_{CPE} = \frac{1}{Q(j\omega)^n} \tag{4}$$

where *Q* is a proportional factor, ω is the angular frequency and *n* is an empirical exponent with values between 0 (ideal resistor) and 1 (ideal capacitor). All samples were fitted by a non-linear function and are presented in Fig. 8. R_g, R_{gb} and R_e are grain resistance, grain boundary resistance and

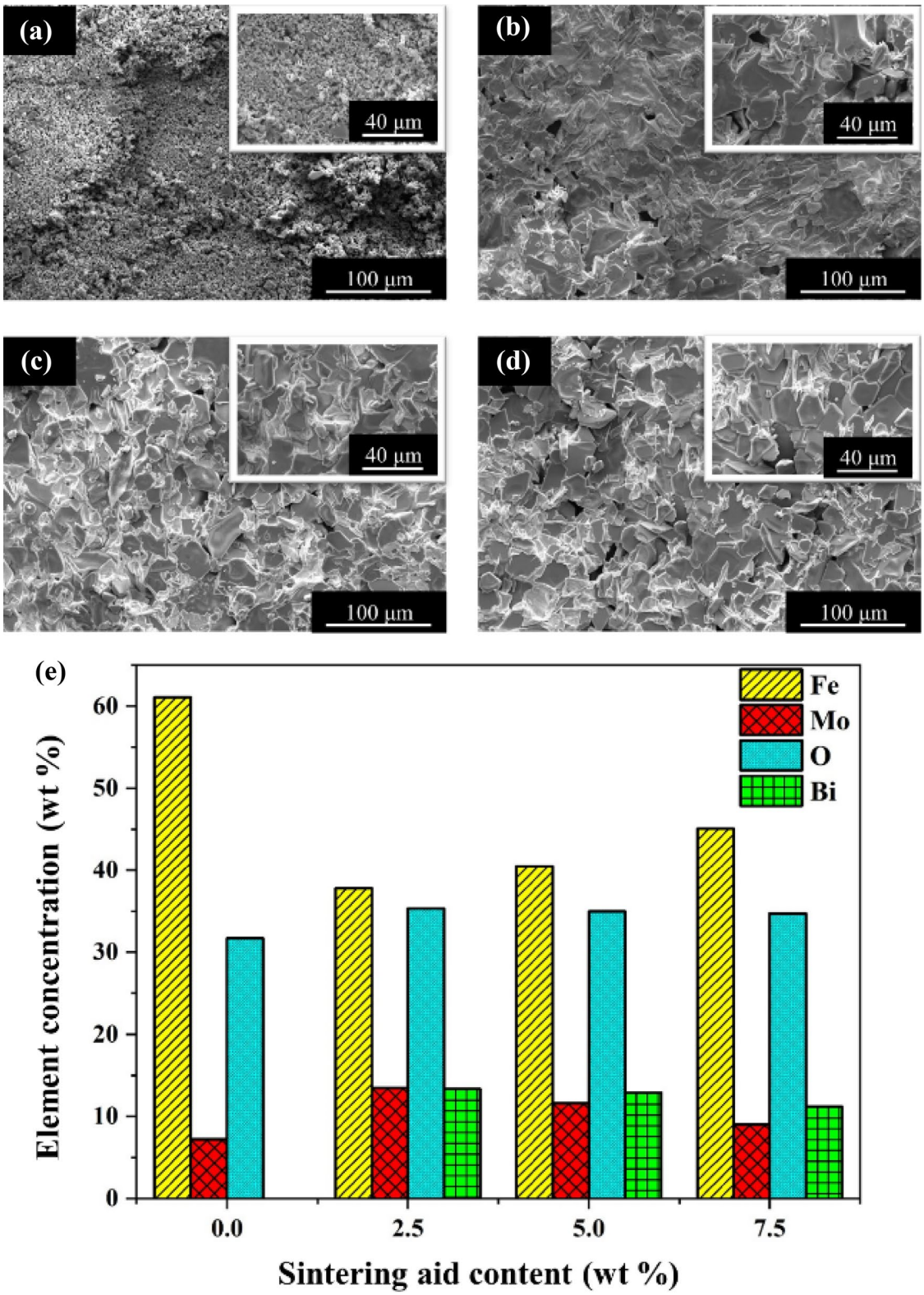

Fig. 4 Surface micrograph of **a** FMO, **b** FMO-2.5, **c** FMO-5.0 and **d** FMO-7.5 pellets. Percentage composition in mass ratio *versus* sintering aid content (**e**)

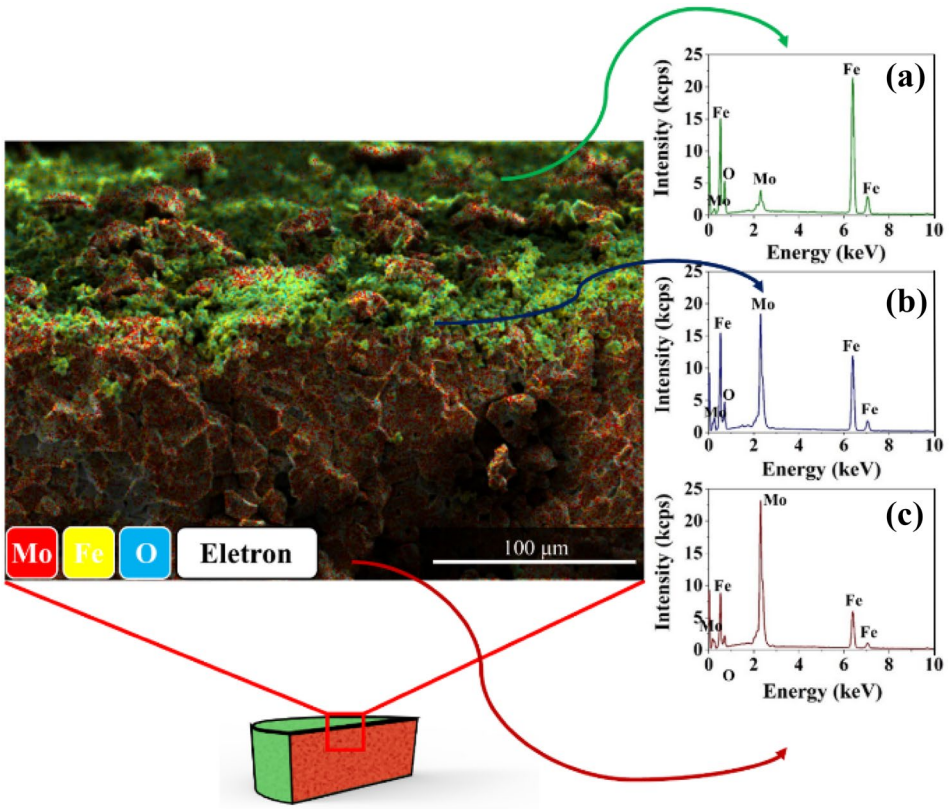

Fig. 5 Cylindrical pellet scheme and EDS spectra of different areas. **a** Surface, **b** surface/inner interface and **c** inner

electrode resistance, respectively, while CPE_g, CPE_{gb} and CPE_e are grain constant phase element, grain boundary constant phase element and electrode constant phase element. Resistive and capacitive contributions of each component (grain, grain boundary and electrode) of the FMO, FMO-2.5, FMO-5.0 and FMO-7.5 are presented in Tables S3, S4, S5 and S6 of ESM, respectively.

As described previously in *Z"* spectra, the resistive contribution of grain, grain boundary and electrode effect decreases with temperature increasing. Grain and electrode are predominantly capacitive due to the fitted parameter *n* (deviation of ideal capacitance) for CPE element with increasing of the temperature [53].

The addition of sintering aid makes the electrode contribution purely resistive, eliminating the capacitive. Moreover, for all samples, the increasing of temperature leads to the decreasing of *n* value for grain boundary contribution, indicating an increasing in resistive contribution of this element. Thermal stability of capacitance (*TCC*) was also determined for all samples using the relation described in Eq. 5 [54].

$$TCC = \frac{C_{100} - C_{25}}{C_{25}.(100 - 25)}.10^6, \quad (5)$$

where C_{100} and C_{25} are the capacitance in 100 and 25 °C respectively. Table 3 presents the TCC in 100 Hz, 1 kHz, 10 kHz and 1 MHz frequencies.

FMO-2.5 presents the highest value of TCC for all frequencies. FMO-7.5 is unstable at low frequencies, presenting 20,747.38 and 18,966.13 ppm.°C^{-1} at 100 Hz and 1 kHz respectively, but is stable at high frequencies. Although FMO, FMO-5.0 and FMO-7.5 presented low value of TCC, at 10 kHz and 1 MHz, according to IEC/EN 60,384–8/21 and EIA-RS-198, FMO, FMO-2.5 and FMO-7.5 are potential to be applied as class 1 capacitor at 10 kHz. These ceramics were also analyzed in a microwave frequency range. The temperature coefficient of resonant frequency (τ_f) was determined using the relation described in Eq. 6 [54].

$$\tau_f = \frac{f_{80} - f_{25}}{f_{25}.(80 - 25)}.10^6, \quad (6)$$

where f_{80} and f_{25} are the resonant frequency at 80 °C and 25 °C, respectively. Table 4 presents the microwave dielectric properties for all samples. Table 4 presents the microwave dielectric properties for all samples. The addition of sintering aid does not imply many changes in microwave dielectric properties of bulks. FMO-2.5 presented the higher ε_r value (9.70) among the samples. Furthermore, FMO-based ceramics have ε_r between 9.3 and 9.7, near of Al_2O_3 ($\varepsilon_r = 9.8$), one of the most important oxides used in industry [55]. All compositions showed low values of *tan δ*, and FMO-2.5 presented the smallest value (6.52×10^{-4}). This phenomenon can be related to the liquid phase of sintering

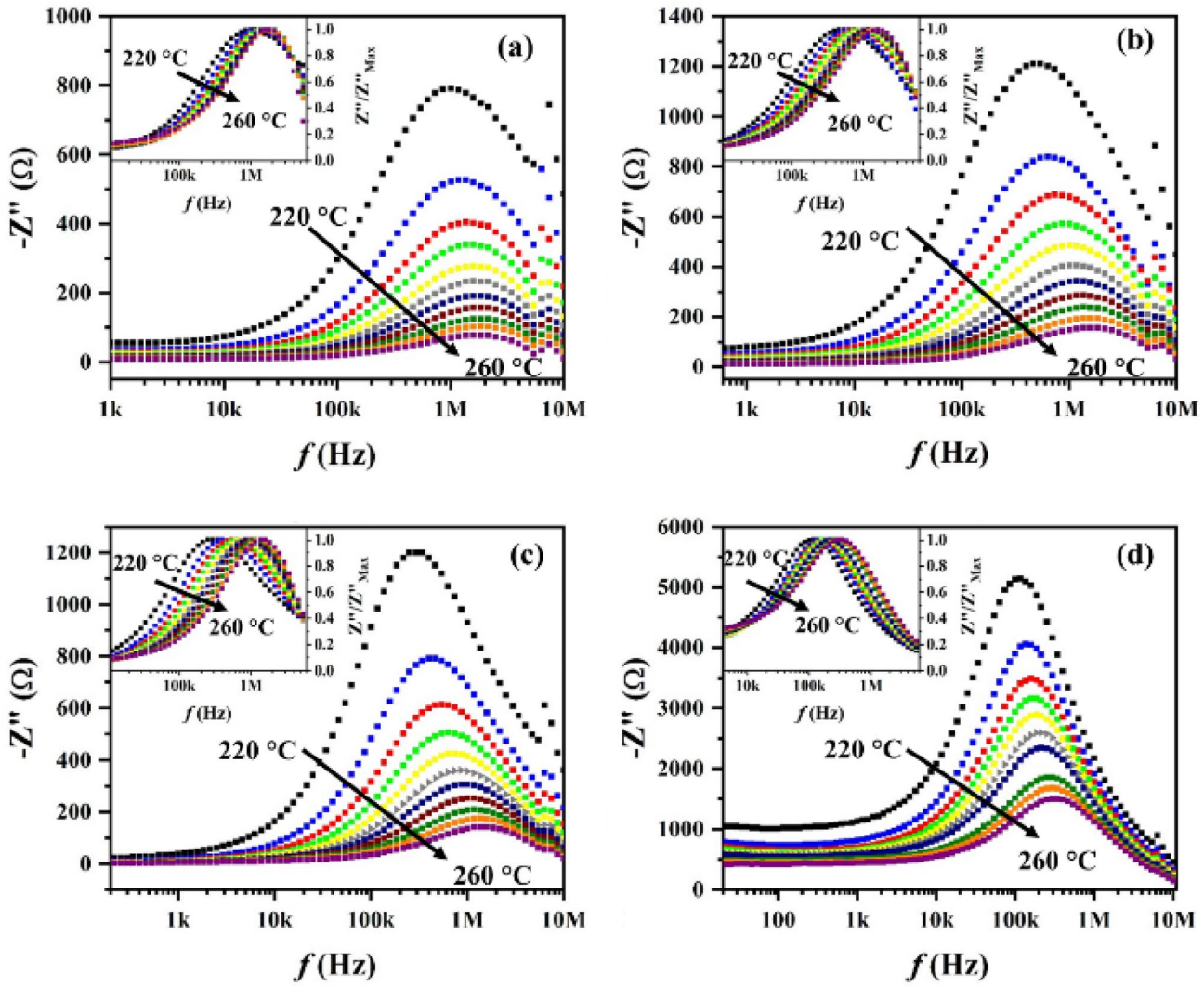

Fig. 6 Z" spectra of **a** FMO, **b** FMO-2.5, **c** FMO-5.0 and **d** FMO-7.5. Normalized *Z"* spectrum (inset)

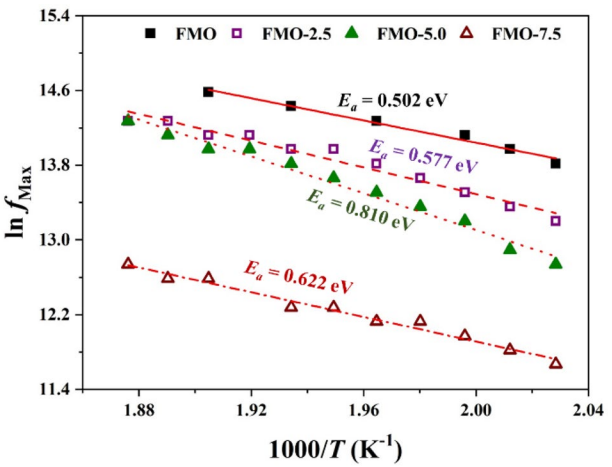

Fig. 7 Activation energy of FMO, FMO-2.5, FMO-5.0 and FMO-7.5

aid between grain interstice [6]. The greatest dielectric loss of FMO can be related to the extrinsic loss due to the smaller grains on the surface of the bulk, as can be seen by SEM images [56]. Although all compositions showed a low dielectric loss, which is required for some applications [5]. Moreover, all the composition presented high values of $Q\,x\,f$, and the FMO-2.5 is the one that presented the highest value of 16,054.24 GHz, which shows its potential use in microwave devices. τ_f values increase in modulus with increasing sintering aid content, except for FMO-7.5 bulk. FMO and FMO-7.5 showed the lower values of τ_f, probably due to the lower quantity of Fe_2O_3 as a spurious phase which presents a τ_f of -66.64 ppm.°C^{-1} [51]. There is a smaller amount of the iron oxide in crystalline form in these samples. As previously discussed in PXRD, FMO-7.5 presents iron oxide in vitreous phase and must probably the τ_f is different from that presented in the literature. However, FMO-2.5 and FMO-5.0

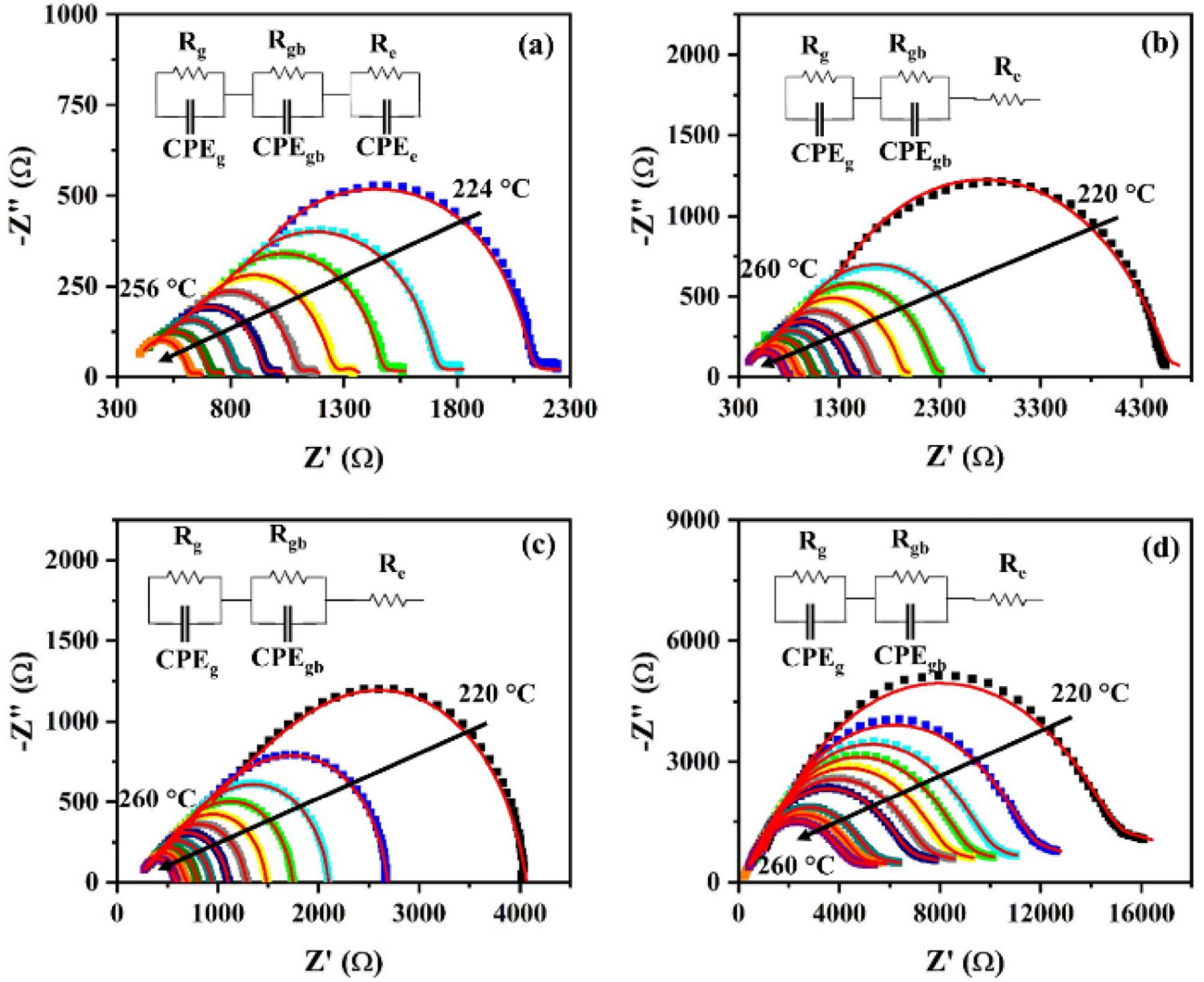

Fig. 8 -Z" *versus* Z' of **a** FMO, **b** FMO-2.5, **c** FMO-5.0 and **d** FMO-7.5

Table 3 TCC of FMO, FMO-2.5, FMO-5.0 e FMO-7.5

TCC (ppm.°C^{-1})				
Composition	100 Hz	1 kHz	10 kHz	1 MHz
FMO	2986.91	4966.44	− 441.12	− 1631.75
FMO-2.5	403,468.83	210,034.36	71,681.96	63,636.36
FMO-5.0	5637.25	4444.44	− 1782.05	− 1956.45
FMO-7.5	20,747.38	18,966.13	− 1821.25	− 2099.24

Table 4 Dielectric properties of FMO, FMO-2.5, FMO-5.0, and FMO-7.5 in the microwave range

Composition	ε_r	*tan δ*	*Q x f (GHz)*	τ_f (ppm.°C^{-1})
FMO	9.33	9.45×10^{-4}	14,132.35	− 6.55
FMO-2.5	9.70	6.52×10^{-4}	16,054.24	− 30.08
FMO-5.0	9.56	6.98×10^{-4}	14,691.35	− 62.99
FMO-7.5	9.49	7.15×10^{-4}	14,439.76	− 4.35

presented the highest values of τ_f. This phenomenon is probably related to the high concentration of Fe_2O_3 in crystalline form, as it was quantified by PXRD analysis [51, 57].

Near-zero τ_f is a very desirable property for resonators and substrates. Recently some researches were taking original strategies to achieve this goal. Castro and coworkers investigated $(Ba_2CoNbO_6)_{1-x}$–$(CaTiO_3)_x$ composite and reached near-zero τ_f at x = 0.37 [58]. Oliveira investigated the effect of $CaTiO_3$ addition in thermal stability of the $BiVO_4$ matrix [59] and Paiva investigated the $Y_3Fe_5O_{12}$–$CaTiO_3$ composite and determined that near-zero τ_f composition [60]. The FMO and FMO-7.5 showed τ_f values of − 6.55 and − 4.35 ppm.°C^{-1}, respectively. Also, they are characterized as near-zero τ_f since their values are

smaller than ± 10 ppm.°C^{-1}. Even though, the FMO presents a τ_f near zero, the formation of a vitreous phase improves the τ_f of the FMO.

4 Conclusion

The purpose of this study was to add sintering aid to improve the dielectric properties of the FMO (ε', tan δ, τ_f), relative density, etc. FMO monoclinic phase has been successfully synthesized via the solid-state route and characterized by PXRD, Mössbauer, and Raman spectroscopy. The sintering process at 800 °C was effective in producing dense solids. The SEM images associated with EDS spectra show that the surface of pellets is rich in Fe because of the thermal decomposition of $Fe_2Mo_3O_{12}$ at high temperatures and MoO_3 volatilization. Although there was decomposition of the surface of the sample due to the volatilization of MoO_3, the inner structure is preserved, and presence of Bi_2O_3–B_2O_3 allows the growth of superficial grains. Nyquist diagrams were observed in a temperature range of 220–260 °C. The grain, grain boundary, and electrode effect contributions were analyzed using an equivalent circuit. Three contributions were obtained from R-CPE to the FMO, while for samples with sintering aid, the capacitive contribution of the electrode vanished away. Furthermore, the Bi_2O_3–B_2O_3 mix increases the resistive contribution of grain in all-ceramic samples compared to FMO. The FMO, FMO-5.0 and FMO-7.5 presented low values of TCC ranging − 441.12 to − 1824.25 ppm.°C^{-1} and − 1631.75 to − 2099.24 at 10 kHz and 1 MHz, respectively. Microwave characterization presented ε_r within 9.3 and 9.7, and all compositions presented *tan δ* at the magnitude order of 10^{-4} and $Q\,x\,f$ values above 14,000 GHz. This implies that they all have the potential to be applied as microwave devices, such as microstrip antenna substrate or dielectric resonator antennas. Moreover, FMO and FMO-7.5 have near-zero τ_f (smaller than ± 10 ppm/°C), making them suitable candidates for dielectric resonator antenna.

Supplementary Information The online version contains supplementary material available at https://doi.org/10.1007/s00339-022-05580-3.

Acknowledgements We gratefully acknowledge the financial support of the following Brazilian agencies for scientific and technological development: CNPq (408790/2016-4), CAPES (Finance Code 001-PROEX 23038.000509/2020-82), and Funcap (PNE-0112-00048.01.00/16). In addition, the authors are also grateful for the Central Analítica-UFC/CT-INFRA/MCTI-SISNANO/Pró-Equipamentos, for providing the equipment and technical support for the experiments involving SEM, Laboratório de Difração de raios-X (UFC), and Laboratório de Espectroscopia Vibracional e Microscopia (UFC).

Data availability Data sharing not applicable to this article as all raw data were generated by the authors.

Declarations

Conflict of interest The authors have no competing interests to declare that are relevant to the content of this article.

References

1. H.-H. Guo, M.-S. Fu, D. Zhou, C. Du, P.-J. Wang, L.-X. Pang, W.-F. Liu, A.S.B. Sombra, J.-Z. Su, A.C.S. Appl, Mater. Interfaces **13**, 912 (2020)
2. J. Ren, K. Bi, X. Fu, Z. Peng, J. Alloys Compd. **823**, 153867 (2020)
3. H. Ren, T. Xie, Z. Wu, F. He, Y. Zhang, S. Jiang, X. Yao, H. Lin, J. Alloys Compd. **797**, 18 (2019)
4. Z.B. Feng, B.J. Tao, W.F. Wang, H.Y. Liu, H.T. Wu, Z.L. Zhang, J. Alloys Compd. **822**, 153634 (2020)
5. M.T. Sebastian, H. Wang, H. Jantunen, Curr. Opin. Solid State Mater. Sci. **20**, 151 (2016)
6. P. Zhang, J. Liao, Y. Zhao, H. Xie, L. Liu, M. Xiao, J. Mater. Sci. Mater. Electron. **28**, 4946 (2017)
7. N. Wei, T. Karaki, T. Fujii, Jpn. J. Appl. Phys. **61**, 1–6 (2022).https://doi.org/10.35848/1347-4065/ac3b22
8. X. Wang, D. Zhang, G. Wang, L. Jin, J. Li, Y. Liao, H. Zhang, S. Wang, Ceram. Int. **46**, 10652 (2020)
9. Z. Xiong, B. Tang, X. Zhang, C. Yang, Z. Fang, S. Zhang, J. Am. Ceram. Soc. **104**, 1726 (2021)
10. R. Peng, H. Su, D. An, Y. Lu, Z. Tao, D. Chen, L. Shi, Y. Li, J. Mater. Res. Technol. **9**, 1344 (2020)
11. G. Shu, F. Yang, L. Hao, Q. Zhang, F. Meng, H. Lin, J. Mater. Sci. Mater. Electron. **30**, 7485 (2019)
12. J. Dhanya, E.K. Suresh, R. Naveenraj, R. Ratheesh, Ceram. Int. **44**, 6699 (2018)
13. H. Li, Z. Huang, L. Cheng, S. Kong, S. Liu, Ceram. Int. **43**, 4570 (2017)
14. S. Hao, D. Zhou, L. Pang, M.-Z. Dang, S.-K. Sun, T. Zhou, S. Trukhanov, A. Trukhanov, S. Sombra, Q. Li, J. Mater. Chem. C **10**(6), 2008–2016 (2022). https://doi.org/10.1039/D1TC05557G
15. R. Zuo, Y. Xu, M. Shi, W. Li, L. He, J. Eur. Ceram. Soc. **38**, 4677 (2018)
16. N. Joseph, J. Varghese, T. Siponkoski, M. Teirikangas, M.T. Sebastian, H. Jantunen, A.C.S. Sustain, Chem. Eng. **4**, 5632 (2016)
17. L.-X. Pang, D. Zhou, C.-L. Cai, W.-G. Liu, Mater. Lett. **92**, 36 (2013)
18. J. Ren, K. Bi, X. Fu, Z. Peng, J. Mater. Chem. C **6**, 11465 (2018)
19. N. Joseph, J. Varghese, M. Teirikangas, M.T. Sebastian, H. Jantunen, Compos. Part B Eng. **141**, 214 (2018)
20. H. Lv, P. Du, L. Luo, W. Li, Mater. Adv. **2**, 2642 (2021)
21. W. Wang, M. Fu, S. Liu, X. Zhang, Y. Wei, G. Li, J. Lumin. **242**, 118536 (2022)
22. W. Sun, Z. Zhang, H. Liu, W. Wang, X. Zeng, J. Alloys Compd. **794**, 1 (2019)
23. G. Zeng, H. Yuan, J. Guo, Q. Sun, Q. Gao, M. Chao, X. Ren, E. Liang, Phys. Chem. Chem. Phys. **22**, 12605 (2020)
24. H. Liu, Y. Wang, F. Hafeez, Z. Zhang, Ceram. Int. **47**, 34687 (2021)
25. T.A. Mary, A.W. Sleight, J. Mater. Res. **14**, 912 (1999)
26. Z.Y. Li, W.B. Song, E.J. Liang, J. Phys. Chem. C **115**, 10 (2011)
27. J.V.B. Moura, G.S. Pinheiro, P.T.C. Freire, J. Mendes Filho, G.D. Saraiva, B.C. Viana, C. Luz-Lima, Vib. Spectrosc. **87**, 88 (2016)
28. Z.Y. Li, W.B. Song, E.J. Liang, J. Phys. Chem. C **115**, 17806 (2011)

29. Z. Zou, Y. Lou, X. Song, H. Jiang, K. Du, C. Yin, W. Lu, X. Wang, X. Wang, M. Fu, Adv. Mater. Interfaces **8**, 2100584 (2021)
30. Y.-S. Lu, Z. Wang, Y.-F. Xu, Q. Liu, G.-R. Qian, Desalin. Water Treat. **57**, 7898 (2016)
31. M.R. Tohidifar, Ceram. Int. **44**, 3699 (2018)
32. S. Le, J. Zhang, X. Zhu, J. Zhai, K. Sun, J. Power Sources **232**, 219 (2013)
33. Y. Pan, J. Yin, K. Zuo, D. Yao, Y. Xia, H. Liang, Y. Zeng, Ceram. Int. **42**, 9222 (2016)
34. C.M. dos Santos, A.F.N. Martins, B.C. Costa, T.S. Ribeiro, T.P. Braga, J.M. Soares, J.M. Sasaki, J. Nanomater. **2016**, 1–9 (2016) https://doi.org/10.1155/2016/1637091
35. C.A. Schneider, W.S. Rasband, K.W. Eliceiri, Nat. Methods **9**, 671 (2012)
36. B.W. Hakki, P.D. Coleman, I.R.E. Trans, Microw. Theory Tech. **8**, 402 (1960)
37. M.A.S. Silva, T.S.M. Fernandes, A.S.B. Sombra, J. Appl. Phys. **112**, 74106 (2012)
38. L.P. Prisco, P.I. Pontón, W. Paraguassu, C.P. Romao, M.A. White, B.A. Marinkovic, J. Mater. Res. **31**, 3240 (2016)
39. Y. Cheng, H. Xiao, W. Guo, W. Guo, Thermochim. Acta **444**, 173 (2006)
40. F. Deng, X. Lin, Y. He, S. Li, R. Zi, S. Lai, J. Forensic Sci. **60**, 1040 (2015)
41. Y.Z. Cheng, M.M. Wu, J. Peng, X.L. Xiao, Z.X. Li, Z.B. Hu, R. Kiyanagi, J.S. Fieramosca, S. Short, Mater. Technol. **23**, 33 (2008)
42. Z. Jirak, R. Salmon, L. Fournes, F. Menil, P. Hagenmuller, Inorg. Chem. **21**, 4218 (1982)
43. S. Yoon, J. Magn. **19**, 323 (2014)
44. V.K. Sharma, G. Klingelhofer, T. Nishida, in Mössbauer spectroscopy: applications, in *chemistry, biology, and nanotechnology*, ed. by V.K. Sharma, G. Klingelhöfer, T. Nishida (Wiley, Hoboken, 2013), pp. 351–389
45. A.K.H. Bashir, C.M. Furqan, K. Bharuth-Ram, K. Kaviyarasu, M.B.T. Tchokonté, M. Maaza, Phys. E Low-Dimens. Syst. Nanostructures **111**, 152 (2019)
46. R. Iordanova, Y. Dimitriev, V. Dimitrov, S. Kassabov, D. Klissurski, J. Non. Cryst. Solids **231**, 227 (1998)
47. Q. Q. Liu, J. Yang, X. N. Cheng, Adv. Mater. Res. **287–290**, 373 (2011)
48. M.K. Meyer, A.J. Thom, M. Akinc, Intermetallics **7**, 153 (1999)
49. J. Sun, T. Li, G.-P. Zhang, Corros. Sci. **155**, 146 (2019)
50. H. Trabelsi, M. Bejar, E. Dhahri, M. Sajieddine, K. Khirouni, P.R. Prezas, B.M.G. Melo, M.A. Valente, M.P.F. Graça, J. Alloys Compd. **723**, 894 (2017)
51. M.A.S. Silva, R.G.M. Oliveira, A.S.B. Sombra, Ceram. Int. **45**, 20446 (2019)
52. J.R. Macdonald, E. Barsoukov, History **1**, 1 (2005)
53. D.V.M. Paiva, M.A.S. Silva, A.S.B. Sombra, P.B.A. Fechine, J. Alloys Compd. **748**, 766 (2018)
54. D. Wang, D. Zhou, K. Song, A. Feteira, C.A. Randall, I.M. Reaney, Adv. Electron. Mater. **5**, 1900025 (2019)
55. H. Wang, J. Chen, W. Yang, S. Feng, H. Ma, G. Jia, S. Xu, J. Eur. Ceram. Soc. **32**, 541 (2012)
56. M.T. Sebastian, *Dielectric materials for wireless communication*, 1st edn. (Elsevier, Amsterdam, 2008), pp. 1–45
57. C.-L. Huang, W.-R. Yang, Y.-R. Chen, J. Alloys Compd. **495**, L5 (2010)
58. A.J.N. de Castro, V.L. Bessa, J.E.V. de Morais, L.P. Silva, R.G.M. Oliveira, J.P.C. do Nascimento, J.C. Sales, M.A.S. Silva, J.C. Goes, D.X. Gouveia, Mater. Res. Bull. **113**, 169 (2019)
59. R.G.M. Oliveira, R.A. Silva, J.E.V. de Morais, G.S. Batista, M.A.S. Silva, J.C. Goes, H.D. de Andrade, I.S.Q. Júnior, C. Singh, A.S.B. Sombra, Compos. Part B Eng. **175**, 107122 (2019)
60. D.V.M. Paiva, M.A.S. Silva, R.G.M. De Oliveira, A.R. Rodrigues, L. Fechine, A.S.B. Sombra, P.B.A. Fechine, J. Alloys Compd. **783**, 652 (2019)